

Dissipationless transport of electrons and Cooper pairs in an electron waveguide

Anil Annadi^{1,2}, Shicheng Lu^{1,2}, Hyungwoo Lee³, Jung-Woo Lee³, Guanglei Cheng^{1,2}, Anthony Tylan-Tyler^{1,2}, Megan Briggeman^{1,2}, Michelle Tomczyk^{1,2}, Mengchen Huang^{1,2}, David Pekker^{1,2}, Chang-Beom Eom³, Patrick Irvin^{1,2}, Jeremy Levy^{1,2*}

¹Department of Physics and Astronomy, University of Pittsburgh, Pittsburgh, PA 15260, USA.

²Pittsburgh Quantum Institute, Pittsburgh, PA, 15260 USA. ³Department of Materials Science and Engineering, University of Wisconsin-Madison, Madison, WI 53706, USA.

*To whom correspondence should be addressed. E-mail: jlevy@pitt.edu

Electrons undergo profound changes in their behavior when constrained to move along a single axis. Theories of one-dimensional (1D) transport of interacting electron systems depend crucially on the sign of the electron-electron interaction. To date, clean 1D electron transport has only been reported in systems with repulsive interactions; SrTiO₃-based heterointerfaces exhibit superconducting behavior with attractive interactions that are manifested far outside the superconducting regime. However, the relatively low mobilities of two-dimensional (2D) complex-oxide interfaces appear to preclude ballistic transport in 1D. Here we show that nearly ideal 1D electron waveguides exhibiting ballistic transport of electrons and non-superconducting Cooper pairs can be formed at the interface between the two band insulators LaAlO₃ and SrTiO₃. Full quantization of conductance is observed for micrometer-length devices, establishing that electron transport takes place with negligible dissipation or scattering. The electron waveguides possess gate and magnetic-field selectable spin and charge degrees of freedom and can be tuned to the one-dimensional limit of a single quantum channel. These complex-oxide-based waveguides provide insights into quantum transport in the extreme 1D limit, in a regime in which electrons have a mutual attraction for one another. The selectable spin and subband quantum numbers of these electron waveguides may be useful for quantum simulation, quantum information processing, spintronics, and sensing.

Electrons confined in one dimension lose nearly all of their recognizable features [1,2]. The electron spin and charge can separate and move independently of one another [3], and the charge itself can fractionalize [4]; however, the conductance remains quantized in units of e^2/h [5]. In well-studied one-dimensional systems such as carbon nanotubes [6], graphene nanoribbons [7], and compound semiconductor nanowires [8,9], electron transport is sensitive to minute amounts of disorder. For example, when 2D semiconductor heterostructures are patterned into 1D channels, the mobility drops tremendously [10]. Theoretically this can be understood within the framework of Tomonaga-Luttinger liquid theory, which predicts that repulsive interactions promote full backscattering from even a single weak impurity [11,12]. Conversely, attractive interactions are predicted to strongly suppress scattering from impurities [12,13].

Oxide heterostructures have added new richness to the field of quantum transport in the last decade. For example, ZnO/(Mn,Zn)O heterostructures have achieved sufficiently high mobility to reveal fractional quantum Hall states [14]. LaAlO₃/SrTiO₃ heterostructures [15] exhibit a wide range of behavior including gate-tunable conducting [16], superconducting [17], ferromagnetic [18], and spin-orbit coupled [19,20] phases. As interesting and rich as its palette of phases may be in terms of exploring new physics in 1D, the electron mobility is still low ($\mu \sim 10^3$ cm²/Vs) compared with high-mobility GaAs/AlGaAs heterointerfaces ($\mu \sim 10^7$ cm²/Vs). Despite the modest mobility of the LaAlO₃/SrTiO₃ 2D interface, there is an increasing body of evidence suggesting that 1D geometries are able to support highly specular or ballistic transport [21-24].

Here we describe transport in ballistic 1D LaAlO₃/SrTiO₃ electron waveguides with reproducible control over subband occupation and spin states. The electron waveguides are created using a well-established conductive atomic-force microscopy (c-AFM) lithography technique [25,26]. Positive voltages applied between the c-AFM tip and the top LaAlO₃ surface produce locally conductive regions at the LaAlO₃/SrTiO₃ interface (illustrated in Fig. 1a), while negative voltages locally restore the insulating phase. The mechanism for writing (erasing) is attributed to LaAlO₃ surface protonation (de-protonation) [27,28]. The protonated LaAlO₃ surface in critical-thickness LaAlO₃/SrTiO₃ heterostructures creates an attractive confining potential that

defines the nanowire. Because the protons are physically separated from the conducting region by a highly insulating LaAlO₃ barrier, this nanofabrication method can be viewed as analogous to the “modulation doping” technique [29] commonly used in III-V semiconductor heterostructures. The separation of dopants from the conducting region minimizes scattering from imperfections. A key difference from III-V nanostructures is the relative proximity between the dopant layer and conducting channel, here only 1.2 nm. Typical nanowire widths at room temperature are $w \sim 10$ nm, as measured by local erasure experiments [25].

The geometry used to investigate electron waveguide transport (Fig. 1a) consists of a nanowire channel of total length L_c , surrounded by two narrow, highly transparent barriers (width $L_b \sim 5 - 10$ nm) separated by a distance $L_s \sim 10 - 1000$ nm. The chemical potential μ of the nanowire segment can be tuned by a side-gate voltage V_{sg} , which is positioned about 800 nm away from the nanowire. Four-terminal transport measurements are carried out at or close to the base temperature of a dilution refrigerator ($T = 50$ mK) and subject to out-of-plane magnetic fields B up to 9 tesla, unless otherwise specified.

The expected properties of an ideal few-mode (i.e., subband) electron waveguide are illustrated in Fig. 1b-g. The conductance of the waveguide depends on the number of accessible quantum channels (shown in Fig. 1d-e as energy-shifted parabolic bands). Fig. 1b,d depict a state in which a single spin-resolved subband is occupied. As the chemical potential μ is increased, more subbands in the nanowire channel become occupied. Fig. 1c,e depict a state in which $N=3$ subbands contribute to transport. Each spin-resolved subband contributes e^2/h to the total conductance (Fig. 1f). The energy at which μ crosses a new subband (at $k_x = 0$) can generally shift in an applied magnetic field due to Zeeman and orbital effects (Fig. 1g).

The experimentally measured conductance of LaAlO₃/SrTiO₃ waveguides is shown in Fig. 2. Here we focus on two distinct devices, device A ($L_c = 500$ nm, $L_s = 50$ nm, $L_b = 20$ nm) and device B ($L_c = 1.8$ μ m, $L_s = 1$ μ m, $L_b = 20$ nm). Figure 2a shows the zero-bias conductance $G = dI/dV$ as a function of side-gate voltage V_{sg} for a sequence of magnetic fields between $B = 0$ T and 9 T. Clear conductance quantization at $G = 2e^2/h$ is visible for magnetic fields above ~ 1 T, and splits into integer multiples of e^2/h , up to $N = 6$. Finite-bias spectroscopy further reveals so-called “half plateaus” due to uneven population of electrons transmitting from source

and drain leads, which is characteristic of very clean transport [30] (see Methods). Further analysis enables the lever-arm ratio ($\alpha \equiv d\mu/dV_{sg}$, where μ is the chemical potential) and g -factor ($g \equiv \mu_B^{-1} d\mu/dB$, where μ_B is the Bohr magneton) for the two devices A(B) to be extracted: $\alpha_{A(B)} = 4.5$ (9.9) $\mu\text{eV/mV}$ and $g_{A(B)} = 0.6$. When only a single barrier is present, no conduction quantization is observed (Fig. 10b) because the tunneling barriers are extremely narrow, in contrast to traditional semiconductor heterostructures. This conclusion is also supported by transport simulations (Fig. 10a,c).

The observed conduction plateaus are attributed to Landauer quantization [5], which depends on the number of available quantum channels (subbands) for conduction. The subband structure of these LaAlO₃/SrTiO₃ electron waveguides is clearly revealed by examining the transconductance $dG/d\mu$ as a function of μ and external magnetic field B (Figs. 2c, d). The transconductance shows an intricate set of bands (dark areas) which mark the boundaries where new subbands become available (as illustrated in Fig. 1g). These bands are separated by light areas ($dG/d\mu \rightarrow 0$) where the conductance is highly quantized. At low magnetic fields (and low μ), the subbands scale roughly as B^2 and become more linear at larger magnetic fields. A pattern of subbands repeats at least twice, spaced by approximately 500 μeV . The transconductance of the two devices A ($L_s = 50$ nm) and B ($L_s = 1$ μm) are remarkably similar, despite the channel length difference and the fact that the coupling constant for the two devices differs by a factor of two. While the lowest $N = 1$ state remains highly quantized for both devices, the plateaus do not fully reach the integer values for higher N for device B.

Many of the features in the transconductance spectra are captured by a waveguide model of non-interacting electrons in a 1D waveguide. The waveguide's confining potential can be regarded as translationally invariant along the propagation direction (x) and convex along the two transverse directions (lateral y and vertical z). Due to the low electron density and the known splitting of the Ti d_{xy} band from d_{xz} and d_{yz} due to interactions with the LaAlO₃ interface [31], we assume that all of the conducting channels are derived from the lower d_{xy} band. We use a potential $U_y = \frac{1}{2} m_y^* \omega_y^2 y^2$ to describe the lateral confinement, where $m_x^* = m_y^*$ is the effective mass in the x - y plane and $\omega_y = \frac{\hbar}{m_y^* l_y^2}$ is the confinement frequency with l_y being the characteristic

width of the waveguide. In the vertical direction, the confinement at the interface is modeled by a half-parabolic potential, namely, $U_z = \frac{1}{2} m_z^* \omega_z^2 z^2$ for $z > 0$ and $U_z = +\infty$ for $z \leq 0$, where $\omega_z = \frac{\hbar}{m_z^* \ell_z^2}$ is the confinement frequency, m_z^* is the effective mass of the d_{xy} band in the z direction, and ℓ_z is the penetration depth into the SrTiO₃. Within this single-particle picture, the full Hamiltonian can be written in the Landau gauge as

$$H = \frac{-\hbar^2(\partial_x - eBy)^2}{2m_x^*} - \frac{\hbar^2 \partial_y^2}{2m_y^*} - \frac{\hbar^2 \partial_z^2}{2m_z^*} + \frac{m_y^* \omega_y^2}{2} y^2 + \frac{m_z^* \omega_z^2}{2} z^2 - g \frac{\mu_B}{2} B \sigma_z, \quad (1)$$

where σ_z is the Pauli matrix. This Hamiltonian is readily solved (see Methods) to yield energy eigenstates $|n, m, s\rangle \otimes |k_x\rangle$ with corresponding energy

$$E_{m,n,s,k_x} = \hbar\Omega \left(n + \frac{1}{2} \right) + \hbar\omega_z \left((2m + 1) + \frac{1}{2} \right) - g\mu_B B s + \frac{\hbar^2 k_x^2}{2m_x^*} \left(1 - \frac{\omega_c^2}{\Omega^2} \right), \quad (2)$$

where $\omega_c = \frac{eB}{m_y^*}$ is the cyclotron frequency, $\Omega = \sqrt{\omega_y^2 + \omega_c^2}$ is the effective frequency of the wire and magnetic field, n (m) enumerates the lateral (vertical) states, and $s = \pm 1/2$ is the spin quantum number. Distinct spin-resolved subbands [32] are associated with the discrete quantum numbers $|n, m, s\rangle$. Figure 3a plots the eigenenergies for parameters that have been adjusted to resemble the experimentally measured transconductance (Fig. 2c). The corresponding wavefunctions $\phi_{n,m,k_x,s}(y, z) \equiv \langle y, z, s; k_x | n, m, s \rangle$ for selected states are illustrated in Fig. 3c. The wavefunctions are displaced magnetically by an amount that depends quadratically on the kinetic energy (Fig. 3b). The set of parameters for device A (B), $\ell_y = 26$ (27) nm, $\ell_z = 8.1$ (7.9) nm, $m_x^* = m_y^* = 1.9$ (1.8) m_e , and $m_z^* = 6.5$ (6.4) m_e is obtained by maximizing agreement with a tight-binding model that includes spin-orbit interactions (see Methods). At low magnetic fields, the energy scales quadratically with magnetic field, being dominated by the geometrical confinement contribution; at higher magnetic fields, the confinement from the cyclotron orbits dominates, producing a linear scaling. The crossover occurs near $\omega_B = \frac{eB}{m_y^*} \sim \omega_y$.

While the single-particle model captures the overall subband structure, clear deviations in the experimental results are apparent. Electron pairing without superconductivity is observed below a critical magnetic field B_p , similar in nature to reports for strongly confined quantum dot

structures [33]. The extracted pairing field for the $|0,0,s\rangle$ states is $B_p \sim 1$ T for device A and B (see Fig. 9 and Methods). In other devices, electron pairing is much stronger. Device C, written on a different canvas, exhibits highly quantized conduction but with a subband structure that differs qualitatively from devices A and B. There are three pairs of subbands that generate $2e^2/h$ steps (Fig. 4a). These pairs unbind at a critical field $B_p \sim 11$ tesla (Fig. 4c, dashed lines). Superimposed over these pairs is a separate subband (with higher curvature) that contributes e^2/h to the conductance (Fig. 4b). At $B \approx 3$ T two paired subbands are superimposed with the unpaired subband, leading to a plateau near $5e^2/h$ (highlighted in red).

Other subband couplings are observed in devices A and B. When subbands with *opposite* spin intersect, e.g. $|1,0,\uparrow\rangle$ and $|0,1,\downarrow\rangle$, they are found to pair re-entrantly before separating again (Figs. 2c,d and Extended Data Figure 5). Such observation is consistent with the phase diagram calculated using a Hartree-Bogoliubov model (Fig. 7). Fitting to a subsequently derived re-entrant pairing model yields a pairing field range $3.3 \text{ T} < B < 3.5 \text{ T}$ and a pairing energy $\Delta_{\text{rp}} = 13 \mu\text{eV}$ for subbands $|1,0,\uparrow\rangle$ and $|0,1,\downarrow\rangle$ in device A (See Methods for details of the fitting methods). When two subbands $|n_1, m_1, s\rangle$ and $|n_2, m_2, s\rangle$ share the *same* spin quantum number s and are nearly degenerate in energy ($E_{m_1, n_1, s} \approx E_{m_2, n_2, s}$), e.g. $|1,0,\uparrow\rangle$ and $|0,1,\uparrow\rangle$, they form an avoided crossing (Figs. 2c,d and Extended Data Figure 4 and 5). Such an effect can arise from electron-electron interactions that give a non-zero coupling term between these two subbands. Alternatively, if both y and z transverse confinement potentials are non-parabolic, avoided crossing can also emerge since the wavefunctions are no longer separable [34,35]. A phenomenological coupling matrix element $\Delta_{1,2} = 20$ (34) μeV can be extracted by fitting to a simple two-level system for these two subbands in device A (B) (see Methods for analysis details).

The observation of quantized conduction in the paired regime ($G = 2e^2/h$ and $|B| < B_p$) signifies that these (non-single-particle) states propagate ballistically, forming an extended state in which electron pairs are bound together while the center-of-mass coordinate remains delocalized. The delocalized nature of these electron pairs appears to compete with superconductivity, which is not observed in the cleanest structures. Conduction quantization with steps of $2e^2/h$, rather than $(2e)^2/h$, is consistent with the notion that dissipation takes place not within the channel itself but in the leads, and that electron pairs unbind before they dissipate energy

[36,37]. The electron density in the ungated leads is higher than in the channel (as depicted in Figs. 1b,d), and electron-electron interaction has been observed to switch abruptly from attractive to repulsive with increasing density [38]. As highlighted in Fig. 4, significant variations in the strength of electron pairing is observed in these ballistic channels, similar to pairing strength variations that have been reported in single-electron transistor geometries [33]. Clearly, there are hidden variables that regulate the strength of electron pairing that have yet to be revealed experimentally.

The experiments described here show that electron waveguides provide remarkably detailed insight into the local electronic structure of these oxide interfaces. The level of reproducibility and reconfigurability illustrated by these experiments represents a quantum leap in control over electronic transport in a solid-state environment. Correlated electron waveguides offer unique opportunities to investigate the rich physics that is predicted for 1D quantum systems [2]. For example, the number of quantum channels can be tuned to the lowest spin-polarized state (with $G = e^2/h$), forming an ideal spin-polarized Luttinger liquid. These 1D channels form a convenient and reproducible starting point for emulating a wider class of 1D quantum systems or for creating quantum channels that can be utilized in a quantum computing platform. While the lowest spin-polarized state is robust to disorder, the higher modes are very sensitive, which makes them potentially useful for nanoscale sensing.

Acknowledgements:

We thank Andrew Daley and Ben Hunt for valuable discussions. This work was supported by ONR N00014-15-1-2847 (J.L.), AFOSR FA9550-15-1-0334 (C.B.E.), AFOSR FA9550-12-1-0057 (J.L., C.B.E.), AOARD FA2386-15-1-4046 (C.B.E.) and grants from the National Science Foundation DMR-1104191 (J.L.), DMR-1124131 (C.B.E., J.L.) and DMR-1234096 (C.B.E.).

Author Contributions

A.A, S.L and M.B performed the experiments, H.L. and J.W.L. grew the samples, G.C. and A.T.T. analyzed the data, A.T.T. and D.P. did theory calculation, G.C., A.T.T., P.I. and J.L. wrote the manuscript, J.L. supervised the whole project, C.B.E. supervised sample growth, all the authors contributed to the discussion of manuscript.

Author Information

Reprints and permissions information is available at www.nature.com/reprints. The authors declare no competing financial interests. Readers are welcome to comment on the online version of the paper. Correspondence and requests for materials should be addressed to J.L. (jlevy@pitt.edu).

APPENDIX A: SAMPLE GROWTH AND PROCESSING

The $\text{LaAlO}_3/\text{SrTiO}_3$ ($\text{LaAlO}_3/\text{SrTiO}_3$) samples were grown by pulsed laser deposition (PLD) technique under conditions that are described in detail elsewhere [39]. The samples used in this study comprise of a 3.4 μm thick LaAlO_3 grown on TiO_2 terminated SrTiO_3 (001). The precise control of LaAlO_3 thickness is achieved by *in-situ* monitoring of the reflection high energy electron diffraction (RHEED) process during the layer by layer growth of LaAlO_3 . To perform electrical measurements, gold (Au) electrodes were made to the $\text{LaAlO}_3/\text{SrTiO}_3$ interface by Ar^+ etching followed by Ti/Au (2 nm/23 nm) sputter deposition. A second set of Au electrodes were patterned on the surface of $\text{LaAlO}_3/\text{SrTiO}_3$ sample that connects to the interface connected Au electrodes at one end and act as contact pads for the wire bonding at another end. Samples were mounted on a chip carrier, and electrical connections were established by Au wire bonding. In our samples, the background resistance between two adjacent interface Au electrodes is $>1 \text{ G}\Omega$ at room temperature, which confirms the insulating ground state of the 3.4 μm $\text{LaAlO}_3/\text{SrTiO}_3$ samples.

APPENDIX B: DEVICE FABRICATION AND MEASUREMENT SETUP

Using c-AFM lithography, nanoscale devices were created using voltages applied via a conductive AFM tip using both writing ($V_{tip} > 0$) and erasing ($V_{tip} < 0$) procedures. Fig. 5a shows the top view of device schematic. First, a set of funnel shape electrodes (not shown, $V_{tip} = 18 \text{ V}$) were created to make the contacts between the patterned Au interface electrodes at one end and nanowires (created with $V_{tip} = 15 \text{ V}$) which were used as current and voltage sensing leads. We apply two-step voltage sequences to create the main channel and barriers as shown in Fig. 5b: first we move the AFM tip with a voltage applied ($V_{tip} = 8 \text{ V}$) across the LaAlO_3 surface to create the main channel, then we repeat the same tip path with a small base voltage ($V_{tip} = 1 \text{ V}$) and apply two negative voltage pulses ($V_{tip} = -7.5 \text{ V}$) to create two transparent barriers. The 1 V tip voltage in the second step is believed to make the surface protons uniform and improves the mobility. The barrier height is determined by the amplitude and duration of the negative pulses. The fabricated device

was immediately transferred to a dilution refrigerator, and cooled to base temperature ($T=50$ mK unless otherwise noted).

Side-gate and back-gate voltages (V_{sg} , V_{bg} respectively) provide fine and coarse tuning of the chemical potential in the nanowire segment. Initial experiments determine a value of V_{bg} that results in suitable leakage-free tuning with V_{sg} . The chemical potential varies linearly with V_{sg} : $\mu = \mu_0 + \alpha V_{sg}$, where α is an empirically determined ‘‘lever arm’’ and μ_0 is a constant offset that depends on V_{bg} .

APPENDIX C: FINITE-BIAS SPECTROSCOPY

Finite-bias spectroscopy is performed through current-voltage (I - V) measurements as function of V_{sg} and B to gain more information of the electron waveguides. As shown in Fig. 6a, a large finite bias ($V_{sd} \geq V_{sd}^*$) can unevenly populate subbands occupied by oppositely travelling electrons, which gives rise to the so-called half plateaus [40]. Fig. 6b is the finite-bias transconductance plot of device A at $B = 7$ T. The light region marked by the numbers is where conductance is quantized. The $0.5e^2/h$ and $1.5e^2/h$ plateaus can be clearly seen in the conductance plot at $V_{sd} = V_{sd}^* = 200 \mu V$ (Fig. 6c). The observation of these half plateaus is indicative of very clean transport of the electron waveguide devices, since back scattering is more likely to happen when unoccupied subbands become available at finite biases.

The finite-bias spectroscopy can be used to extract the lever-arm α , which converts gate voltage to chemical potential. As illustrated in Fig. 6b, the black crossing ($V_{sd}^* = 200 \mu V$, $V_{sg} = 80 mV$) marks the transition from one subband to another due to the bias. At this condition, the energy gain induced by the bias V_{sd}^* should equal to subband spacing marked by $\alpha \Delta V_{sg}$ at zero bias, namely $eV_{sd} = \alpha \Delta V_{sg}$. Then $\alpha = eV_{sd}^*/\Delta V_{sg}$ can be precisely extracted by the slope of the $V_{sd}^* - \Delta V_{sg}$ plot at different magnetic fields (Fig. 6d). For device A, α_A is found to $4.5 \mu eV/mV$, and the fitted linear curve passes across zero as supposed. Similarly, $\alpha_B = 9.9 \mu eV/mV$ can be extracted for device B, suggesting a stronger coupling of side gate to the waveguide due to the larger size.

The Zeeman splitting between two spin-resolved subbands $|0,0,\uparrow\rangle$ and $|0,0,\downarrow\rangle$ can be used to extract the electron g factor. Fig. 6d shows the energy splitting (eV_{sd}^*) between these two subbands at various magnetic fields, where spin degeneracy is moved. Then the g factor is given by $g = \frac{eV_{sd}^*}{\mu_B B}$, where μ_B is the Bohr magneton. And the extracted g factors for device A and B are (within measurement error) the same: $g_{A(B)} = 0.6$.

APPENDIX D: FURTHER DETAILS ON WAVE FUNCTION THEORY

When a perpendicular magnetic field applied to the electron waveguide, the effect is twofold: It provides an additional Zeeman energy of $E_z = g\mu_B B$ that results in spin splitting of subbands without altering the 1D nature of the transport which arises from the transverse confinement of electrons. At sufficiently large magnetic fields where the magnetic length is smaller than the device width, the cyclotron motion of the electrons becomes considerable and results in the formation of additional magneto electric subbands. This effect appears as the transition from parabolic to linear behavior of the bands in the transconductance data at high magnetic fields (Figs. 2b, d). Thus, features which exhibit this process must arise from the confinement of the waveguide and give us the quantum number n labelling the transverse (y) subbands. These low-energy excitations are observed to repeat with a large energy separation between each set. The energy difference between these repetitions is large and insensitive to the magnetic field, leading to the conclusion that these sets must arise from the confinement of the electrons to the interface. The regularity of these repetitions then lead us model this as a half-parabolic potential, giving the quantum number m labelling the vertical (z) subbands.

The Hamiltonian and eigenenergies for this model are given in Eqs. (1) and (2) in the main text. The corresponding eigenstates shown in Fig. 3c are given by

$$\psi_{n,m,k}^\sigma(x, y, z) = N_{n,m,k} e^{ikx} e^{-\frac{m_y^* \Omega}{4\hbar} \left(y - \frac{\hbar \omega_c^2}{m_y^* \Omega} k \right)^2} H_n \left(\sqrt{\frac{m_y^* \Omega}{\hbar}} \left(y - \frac{\hbar \omega_c^2}{m_y^* \Omega} k \right) \right) e^{-\frac{m_z^* \omega_z}{4\hbar} z^2} H_{2m+1} \left(\sqrt{\frac{m_z^* \omega_z}{\hbar}} z \right) \quad (\text{S1})$$

with $H_n(x)$ being the Hermite polynomials. As the energy depends on ω_y and m_y^* separately, we are able to find ℓ_y and m_y^* by fitting the single particle spectrum of the $k = 0$ subbands to the transconductance peaks measured in the devices. As ℓ_z and m_z^* only

appear in the energy through ω_z , this process is unable to find the effective z-direction confinement length or effective mass. Instead, these values may be found by modelling the suppression of the Lande g -factor by crystal effects.

Due to atomic spin-orbit coupling, the g -factor is suppressed from its value for free electrons to $g \approx 0.6$, as measured here. We can use this suppression to fit ℓ_z and m_z^* for the single particle model. To see these effects, we start with a tight binding Hamiltonian which includes all three Ti t_{2g} orbitals and spin-orbit coupling between these orbitals with an atomic spin-orbit coupling factor of $\Delta_{aso} = 19.3$ meV [41]:

$$\begin{aligned}
H = \sum_{i,j,k,s} \left[\sum_{\alpha} \left(-t_x^{\alpha} e^{\frac{i\pi B_j d^2}{\Phi_0}} a_{i,j,k}^{\alpha s \dagger} a_{i+1,j,k}^{\alpha s} - t_y^{\alpha} a_{i,j,k}^{\alpha s \dagger} a_{i,j+1,k}^{\alpha s} - t_z^{\alpha} a_{i,j,k}^{\alpha s \dagger} a_{i,j,k+1}^{\alpha s} \right) \right. \\
\left. + \frac{\Delta_{aso}}{2} \left(-i\sigma_y a_{i,j,k}^{d_{xy}s \dagger} a_{i,j,k}^{d_{yz}s} + i\sigma_x a_{i,j,k}^{d_{xy}s \dagger} a_{i,j,k}^{d_{xz}s} + i\sigma_z a_{i,j,k}^{d_{yz}s \dagger} a_{i,j,k}^{d_{xz}s} \right) + h. c. \right] \\
+ \sum_{i,j,k,s,\alpha} \left[\left(\frac{m_y^{d_{xy}*} \omega_y^2}{2} (jd)^2 + \frac{m_z^{d_{xy}*} \omega_z^2}{2} (kd)^2 + 2t_x^{\alpha} + 2t_y^{\alpha} + 2t_z^{\alpha} \right) a_{i,j,k}^{\alpha s \dagger} a_{i,j,k}^{\alpha s} + \frac{g}{2} \mu_B B \sigma_z a_{i,j,k}^{\alpha s \dagger} a_{i,j,k}^{\alpha s} \right], \quad (S2)
\end{aligned}$$

where $t_j^{\alpha} = \frac{\hbar^2}{2m_j^{\alpha*} d^2}$ is the hopping parameter for the α band in the j direction with effective mass $m_j^{\alpha*}$ and interatomic spacing d and $a_{i,j,k}^{\alpha s(\dagger)}$ destroys (creates) an electron in the α orbital with spin s at the site i, j, k . (A term describing the chemical potential is suppressed.) Since the potentials are described by electrostatic effects, they should have the same characteristic shape for all bands and thus appear the same as in the Hamiltonian Eq. (1) in the main text for all bands. The band structure of this system is found using the KWANT package [42]. We can now fit both m_z^* and ℓ_z using the observed ω_z by tuning $m_z^{d_{xy}*}$ until the effective g -factor of the model agrees with experiment. As we know ω_z from fitting the single-particle $k = 0$ subbands to the transconductance data, we are then able to calculate ℓ_z . In addition to the suppression of the g -factor, this Hamiltonian introduces an effective Rashba spin-orbit coupling in the d_{xy} band which is not observed experimentally due to pairing.

APPENDIX E: ELECTRON-ELECTRON INTERACTION ANALYSIS

In the experimental data, there are clear avoided crossings when energy levels with the same spin and different subbands intersect. Within the model presented above, there are no unaccounted for single-particle terms which may couple these states. The Rashba spin-orbit coupling arising from the confinement of the wire may couple two states with different m and n , but it may not couple states with like spin. If, however, the waveguide were asymmetric in a manner dependent upon both y and z , then such a perturbation could couple these states. Another possibility is electron-electron interactions with the filled k -subbands in the occupied lower subbands can give rise to such a coupling.

To model the avoided crossings and fit the experimental data, a simple two-level effective Hamiltonian of the form

$$H_{\text{eff}} = \begin{pmatrix} E_1 & \Delta_{1,2} \\ \Delta_{1,2} & E_2 \end{pmatrix} \quad (\text{S3})$$

is used, where $\Delta_{1,2}$ couples two states E_1 and E_2 . With the unperturbed energies of the two levels on the diagonal, the avoided crossing can then be found by diagonalizing the matrix, which gives the eigenstates

$$E_{AV\pm} = \frac{1}{2}(E_1 + E_2) \pm \frac{1}{2}\sqrt{(E_1 - E_2)^2 + 4\Delta_{1,2}^2}. \quad (\text{S4})$$

As shown in Fig. 8a, we approximate the single particle energy eigenvalue E_i with a linear field dependence $E_i = k_i B + b_i$ in relatively high magnetic fields (cyclotron frequency $\omega_c \gg \omega_y$), where k_i and b_i are constants and $i = 1, 2$. The detailed fitting parameters for two avoided crossings in device A and B are shown in Table 1.

We also model the effects of inter-subband interactions in the neighborhoods of the points in the energy-magnetic field transconductance diagram where two subbands with opposite spins cross. These crossing points occur when the bottom of two transverse bands (i.e. at zero-bias) becoming degenerate, e.g. $E_{|0,1,\downarrow,k=0\rangle} = E_{|1,0,\uparrow,k=0\rangle}$. We note that the phase diagram of attractive Fermions in one dimension has been extensively studied previously using both the Bethe Ansatz approach [43] (for the case of equal masses) and numerical

approaches [44,45] (for the case of unequal masses). Here, we obtain a mean-field phase diagram that is both consistent with previous results and illuminates the physical origins of the features observed in transport experiments. We expect that the inter-subband attraction has two effects: the attraction tends to pull down the upper subband and promote the formation of inter-subband pairs. We expect that pairs should be particularly stable near the crossing points as (a) kinetic energy of the zero momentum pairs is low (i.e. $E_F \approx E_{|0,1,\downarrow,k} \approx E_{|1,0,\uparrow,-k}$); (b) the density of states is high due to the van Hove singularity at the band bottom (which is further enhanced by the magnetic field).

We use a mean-field Hartree-Bogoliubov model to quantitatively capture the energy shift of the subbands and the inter-subband pair formation. In this model, the quasi-particle energies are described by the single-particle Hamiltonian

$$\begin{pmatrix} \xi_{1,k} + \Sigma_1 & 0 & 0 & \Delta_{rp} \\ 0 & -(\xi_{1,k} + \Sigma_1) & \Delta_{rp} & 0 \\ 0 & \Delta_{rp} & \xi_{2,k} + \Sigma_2 & 0 \\ \Delta_{rp} & 0 & 0 & -(\xi_{2,k} + \Sigma_2) \end{pmatrix} \psi_{\beta,k} = E_{\beta,k} \psi_{\beta,k}, \quad (\text{S5})$$

where we use the $\{c_{1,k}, c_{1,k}^\dagger, c_{2,-k}, c_{2,-k}^\dagger\}$ basis, $\{1,2\}$ are the subband labels, $\psi_{\beta,k}$ and $E_{\beta,k}$ are the quasi-particle wave functions and eigenenergies, $\xi_{\alpha,k}(\mu, B)$ corresponds to the non-interacting energy of an electron in the transverse subband α with momentum k along the wire, in magnetic field B , and chemical potential μ (that is tuned by V_{sg}). $\Sigma_1, \Sigma_2, \Delta_{rp}$ are the mean fields that must be found self-consistently. Σ_α represent the Hartree shifts due to the electrons in the opposite subband $\bar{\alpha}$:

$$\Sigma_\alpha = U_H \int \frac{dk}{2\pi} \langle c_{\bar{\alpha},k}^\dagger c_{\bar{\alpha},k} \rangle \quad (\text{S6})$$

and Δ_{rp} represents the re-entrant pairing field

$$\Delta_{rp} = U_B \int \frac{dk}{2\pi} \langle c_{2,-k} c_{1,k} \rangle. \quad (\text{S7})$$

For concreteness, we have made the minimal assumption that the interactions are momentum-independent (i.e. local in real space) when writing the mean fields. We caution that a nonzero value of Δ should not be interpreted as a signature of superconductivity but only as a signature of pair formation as we are working in one dimension. Finally, when

computing the matrix elements, we must keep in mind that the basis we are using is twice as big as the physical basis and consequently, quasi-particle wave functions come in conjugate pairs. Only one member of the pair should be used (e.g. the one that has the positive eigenvalue and thus corresponds to the quasi-particle creation operator).

We solve the Hartree-Bogoliubov model self-consistently to obtain a phase diagram near the crossing point of the $|0,1,\downarrow\rangle$ and $|1,0,\uparrow\rangle$ subbands (see Fig. 7). The locations of the non-interacting subbands are plotted with dashed lines. By turning on the attractive inter-subband interaction, the Hartree shift tends to pull down the upper subband away from the crossing point; and pairing prevails closer to the crossing point which results in the merger of the two subbands into a single paired subband. We expect that these qualitative predictions are generic of systems with attractive inter-band interactions and not particularly sensitive to the assumptions that we have made: i.e. using the Hartree-Bogoliubov model with local interactions.

Provided the phase diagram in Fig. 7, we use a phenomenological model containing the phase boundaries (solid blue lines in Fig. 7) to describe the re-entrant pairing. The basic scenario is when two subbands $E_1(=k_1B + b_1)$ and $E_2(=k_2B + b_2)$ with opposite spins are tuned closely in energy, they combine as an electron pair and break until the energies are tuned further away. These two subbands would simply cross (red dashed lines) if there were no electron-electron interaction. In the presence of the attractive pairing interaction, the higher energy subband undergoes an energy shift of $-2\delta_{1(2)}$ so that it can be written as $E'_{1(2)} = k_{1(2)}B + b_{1(2)} - 2\delta_{1(2)}$. And a middle section representing the paired phase emerges. The re-entrant pairing energy Δ_{rp} can then be extracted: $\Delta_{rp} = \delta_1 + \delta_2$.

Fig. 9 shows signatures of electron-electron interaction in device A. In the context of Fig. 4 in the main text, the critical magnetic field $B_p \sim 1$ T for pairing of subband $|0,0,\downarrow\rangle$ and $|0,0,\uparrow\rangle$ is low compared to device C, but still much higher than the upper critical field H_{c2} (marked by green lines). The avoided crossing is fitted according to model described in Eqs. S3,S4 and Fig. 8a, with $\Delta_{1,2} = 20$ μeV (marked by solid blue lines). The actual subband structure is influenced by the collective effect of both re-entrant pairing and avoided crossing. For example in device A, subband $|1,0,\downarrow\rangle$ re-pairs with subband $|0,1,\uparrow\rangle$

when $3 T < B < 4 T$, but repels with subband $|0,1, \downarrow\rangle$ when $4 T < B < 6 T$. As shown in Figs. S4c, the E_1 trace is further shifted up by repelling subband $|1,0, \downarrow\rangle$ and turned to E_{AV+} . To correctly extract the re-entrant pairing energy, we also include the influence to avoided crossing in the fitting. Nevertheless, the discontinuity when subband $|0,1, \uparrow\rangle$ and $|1,0, \downarrow\rangle$ cross each other is a clear signature of re-entrant pairing. The detailed fitting parameters are shown in Table 2.

APPENDIX F: SINGLE BARRIER VS DOUBLE BARRIERS

In GaAs-based heterostructure devices, the number of transverse channels that are transmitted through a quantum point contact is typically controlled by a split topgate. In the case of electron waveguides at the LaAlO₃/SrTiO₃ interface, the channel width is determined by the c-AFM lithography writing parameters [25]; V_{sg} does not appreciably alter the characteristic width of the potential. Instead, V_{sg} tunes the chemical potential of the channel (with length L_S), with negligible effects on the grounded leads, as shown in Figs. 1b-e in the main text.

To examine this numerically, we look at the simplest case where the barriers do not disrupt the characteristic potentials of the quantum waveguide and only act as regions in which the chemical potential is continuously changed from that in the leads to that set by V_{sg} . For spinless particles, we may write a simple tight-binding Hamiltonian of the form

$$H = \sum_{i,j} \left[t_x^{dxy} \left(e^{\frac{i\phi_B j d^2}{\Phi_0}} a_{i,j}^\dagger a_{i+1,j} + a_{i,j}^\dagger a_{i,j+1} + h.c. \right) + \left(4t_x^{dxy} + \frac{m_y^* \omega_y^2}{2} (jd)^2 - V_B(id, \mu) \right) a_{i,j}^\dagger a_{i,j} \right] \quad (\text{S8})$$

where $V_B(x, \mu)$ is the chemical potential along the waveguide with μ begin chemical potential of the separated region. This function smoothly connects the chemical potential of the lead (chosen to be $4t_x^{dxy}$ so all subbands are occupied in the leads) to the chemical potential μ set by V_{sg} in the separate region over a characteristic length $\frac{L_b}{2}$ at the beginning and end of a region with characteristic length L_S .

Using the KWANT package to calculate the transport properties of such a system, a single barrier ($L_S = 0$) device does not show quantization at any μ or magnetic field as seen in Fig. 10a. This is what we expect from our model where a single barrier allows continuous tunneling between the leads which may be continuously tuned by changing the barrier height, as experiments show in Fig. 10b. Finally, when two barriers are examined ($L_S > 0$), quantized conductance appears as the magnetic field is increased in Fig. 10c, in agreement with the experimental data in Fig. 2 of the main text.

APPENDIX G: CRITICAL PAIRING MAGNETIC FIELD

The spin degeneracy for the same orbital (especially the lowest orbital $|0,0,s\rangle$) is observed to be only removed after certain critical magnetic field B_p . This is consistent with previously reported phase of electron pairing without superconductivity. For device A and B, $B_p \sim 1$ T is relatively low compared to typical values 2-7 T. However, large variation of B_p is observed, as shown in Fig. 11 for additional devices. No specific characteristic length dependence of B_p is concluded, rather the large B_p variation is dependent on the local electronic structure of LaAlO₃/SrTiO₃ interface.

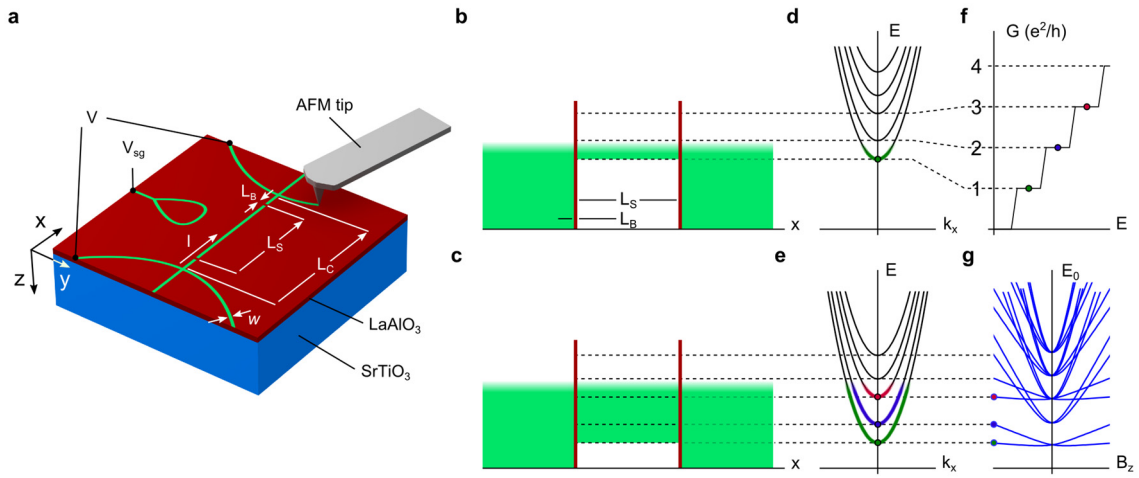


Figure 1 | Expected transport characteristics of electron waveguides. **a**, Schematic of LaAlO₃/SrTiO₃ electron waveguides fabricated by c-AFM lithography. Two barriers, formed by negative AFM tip pulses, surround the main channel, enabling the subbands in the waveguide to be tuned by V_{sg} . **(b and c)** Energy diagrams of the waveguide for two different values of chemical potential μ , which is controlled by V_{sg} . For **b**, a single subband is occupied, while for **c** three subbands are occupied. **(d and e)** depict the corresponding energy subbands corresponding to **b** and **c**. Thick colored bands indicate occupied states. **f**, Zero-bias conductance quantization as a function of chemical potential. **g**, Waveguide subband structure as a function of magnetic field and energy.

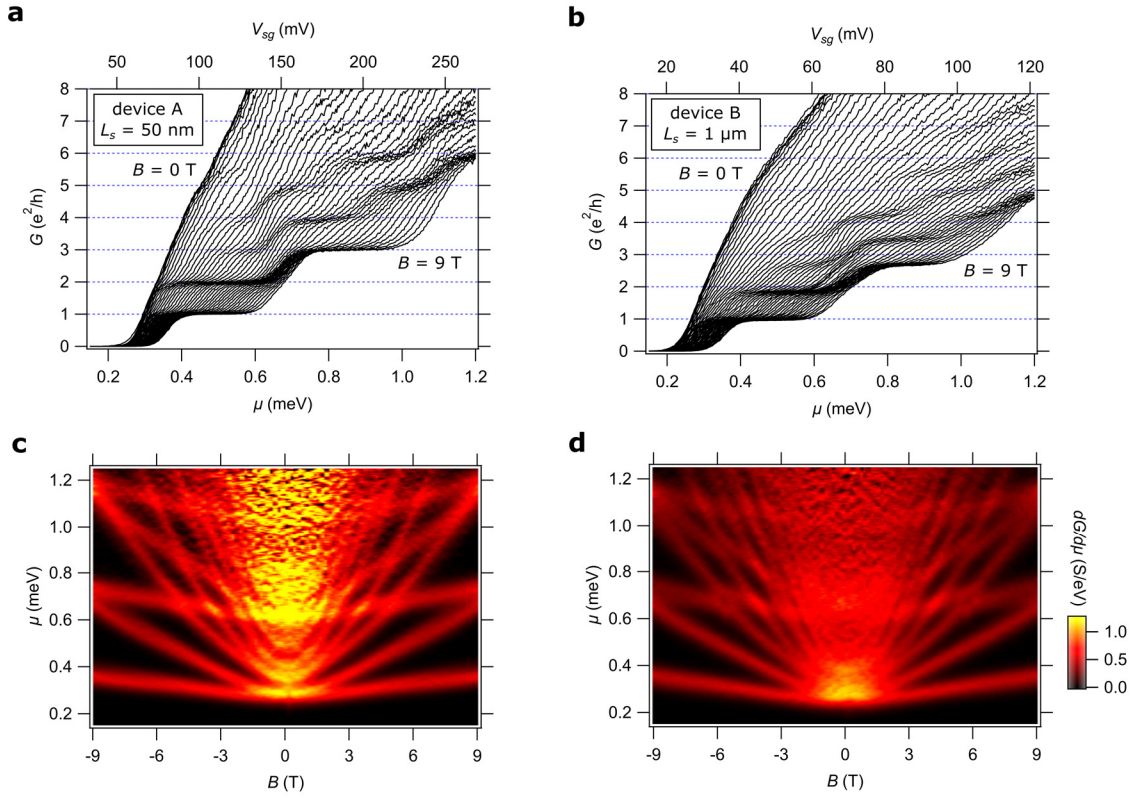


Figure 2 | Transconductance of device A and B. (a and b) Zero-bias conductance of device A ($L_S = 50$ nm) (a) and device B ($L_S = 1000$ nm) (b) as a function of chemical potential μ and magnetic fields B in the range 0-9 T. (c and d) Transconductance $dG/d\mu$ shown as a function of μ and B for device A (c) and device B (d). Each dark band marks the crossing of a subband. The revealed subband structures show remarkable similarity between these two devices.

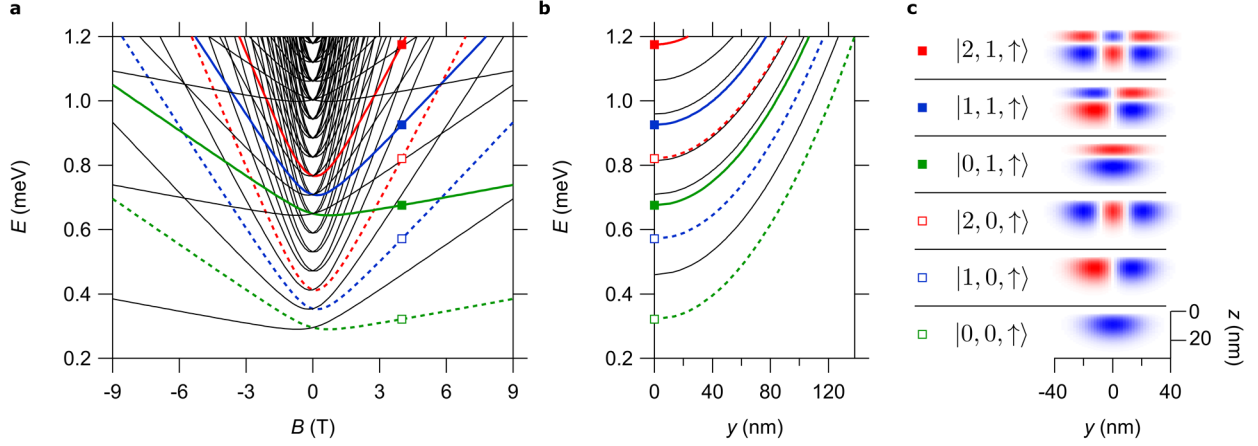


Figure 3 | Non-interacting waveguide model. **a**, Eigenenergies for a quantum wire for the Hamiltonian described in Eq. (1) are plotted as a function of magnetic field B . Selected spin-up states are highlighted in color. **b**, Magnetically induced displacement of these states along the y direction as a function of eigenstate energy for $B = 4$ T. **c**, Six corresponding wavefunctions, labeled by $|n, m, s\rangle$, at $k_x = 0$ and $B = 4$ T. Red and blue colors indicate opposite sign of the wavefunction.

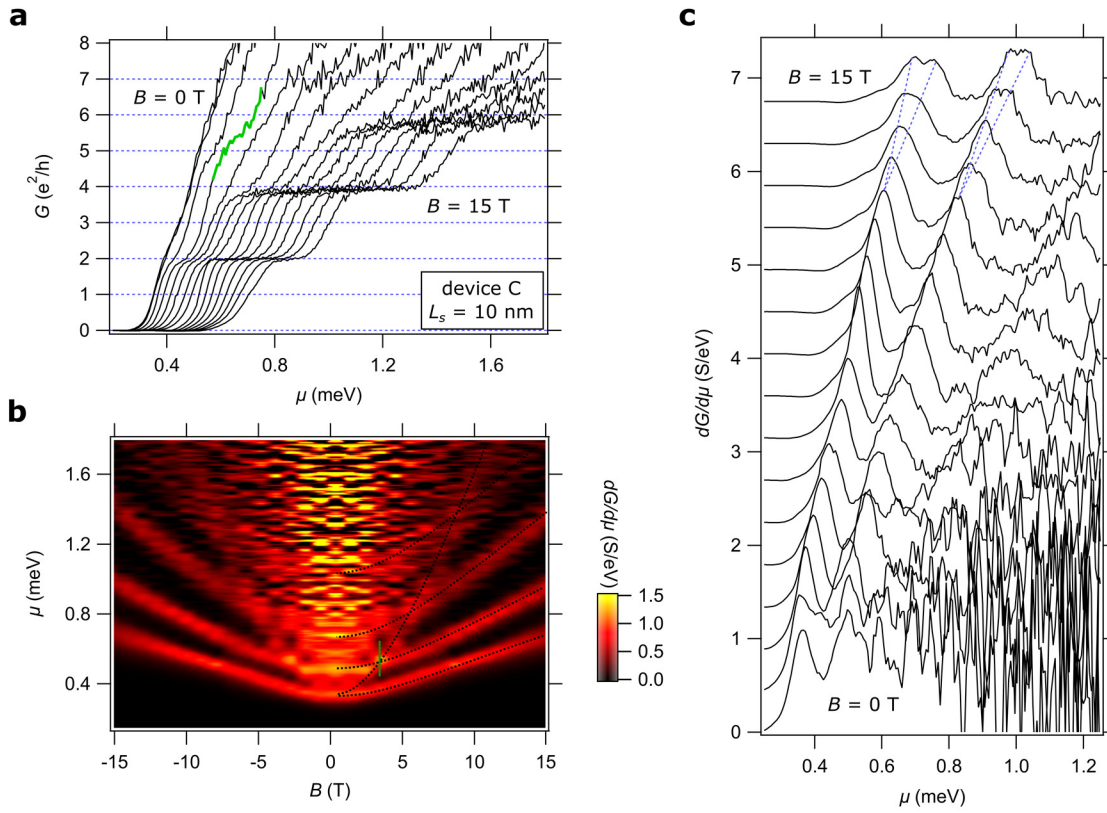


Figure 4 | Strongly paired electron waveguides. **a**, Conductance of device C ($L_s = 10$ nm) versus chemical potential for magnetic fields ranging from 0 T to 15 T. This device shows strong electron pairing and associated $2e^2/h$ conductance steps. **b**, Transconductance plot shows three strongly paired states and a superimposed state with higher curvature associated with a conductance of e^2/h . The value of the later state can be seen at $B = 3$ T in the conductance curve in panel **a** (highlighted in green) where it combines with the second strongly paired subband into a plateau near $5e^2/h$. **c**, Linecuts of transconductance plotted at magnetic fields from 0 T to 15 T in 1 T steps. The $2e^2/h$ peaks split above a pairing field $B_p \sim 11$ T, as indicated by the dashed lines.

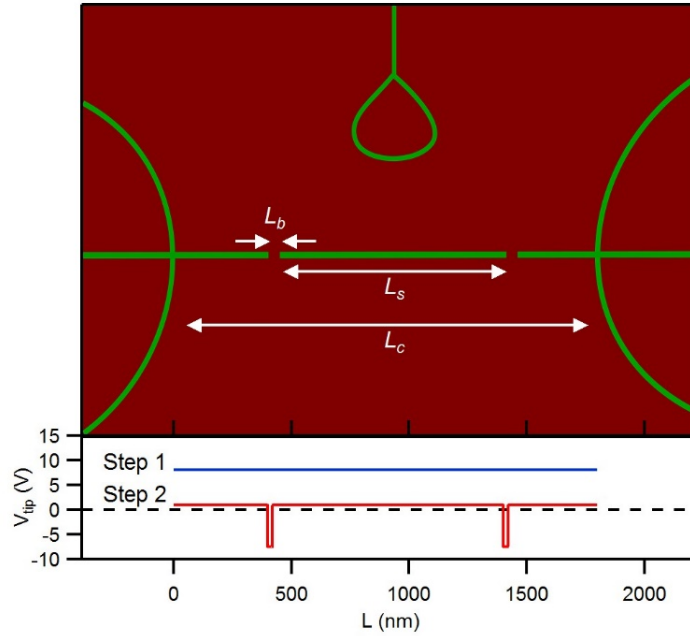


Figure 5 | Device schematic and writing voltage steps taking device B as an example. Top panel: top view of device schematic as shown in Fig. 1A. Bottom panel: Two step voltage sequences which define L_b , L_s and L_c . The main channel is first written with $V_{tip} = 8$ V (blue curve), then the tip repeats the same path with $V_{tip} = 1$ V, and two pulses with $V_{tip} = -7.5$ V that effectively two small barriers of width around 20 nm (red curve).

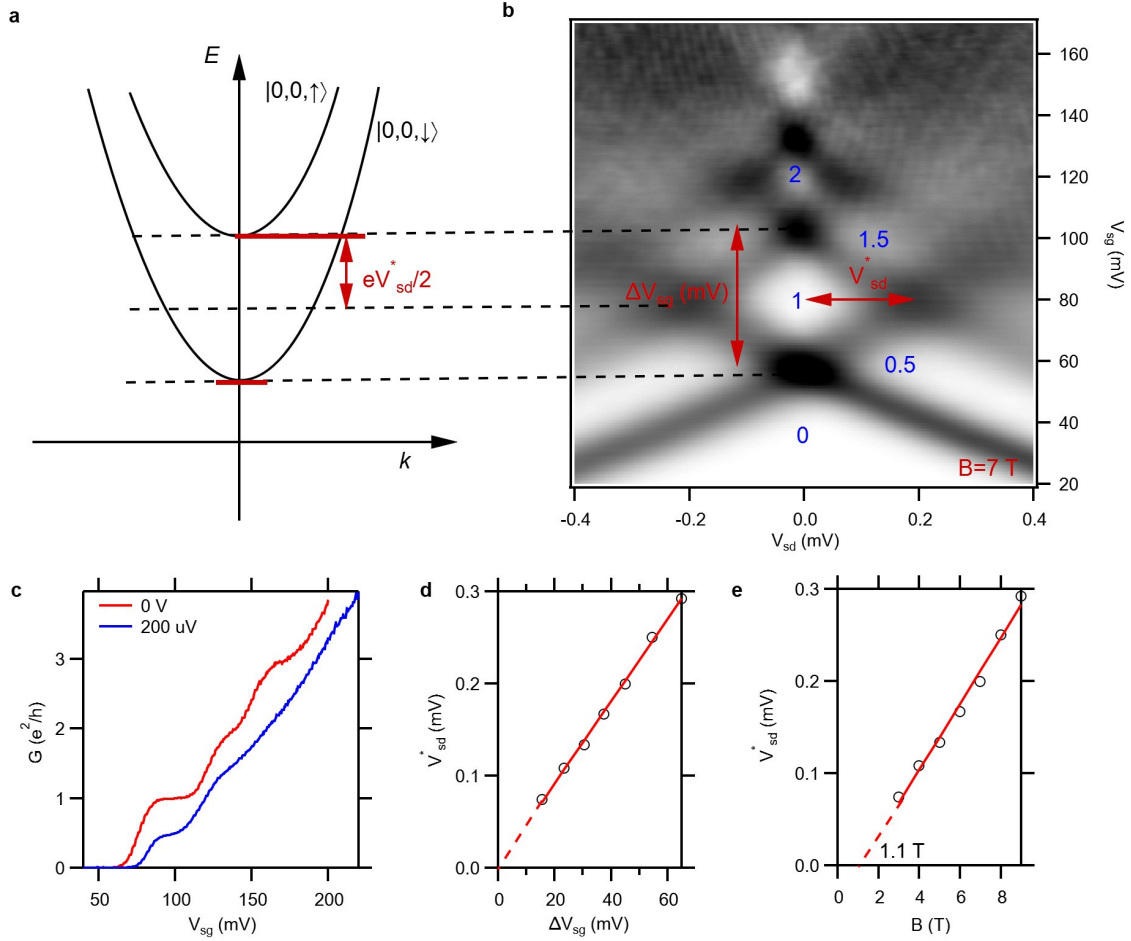


Figure 6 | Finite bias analysis. **a**, Illustration of electron occupation of subbands $|0,0,\downarrow\rangle$ and $|0,0,\uparrow\rangle$ at a finite bias V_{sd} . The application of V_{sd} alters the chemical potentials of drain (μ_d) and source (μ_s) to $E_F \pm eV_{sd}/2$. The energy difference $\mu_d - \mu_s = eV_{sd}^*$ (as indicated by two red lines) equals the subband spacing between subbands $|0,0,\downarrow\rangle$ and $|0,0,\uparrow\rangle$. When $V_{sd} < V_{sd}^*$, electrons travelling in opposite directions occupy the same subband $|0,0,\downarrow\rangle$ with conductance quantized to e^2/h . When V_{sd} reaches $|V_{sd}^*|$ ($-|V_{sd}^*|$), subband $|0,0,\uparrow\rangle$ becomes available for electrons transmitting from drain (source) and gives rise to half plateau conductance ($1.5 e^2/h$). **b**, Transconductance map of device A as a function of V_{sd} and V_{sg} at $B = 7$ T. Each dark band marks the transition between conductance plateaus which are labelled by blue numbers. According to **a**, the conversion factor α can be extracted through a simple relation $V_{sd}^* = \alpha \Delta V_{sg}$. **c**, G vs V_{sg} curves of zero bias ($V_{sd} = 0$ V) and finite bias ($V_{sd} = V_{sd}^* = 200$ μ V) at $B=7$ T. Half plateaus are clearly visible at finite bias (blue curve). **d**, V_{sd}^* dependent on ΔV_{sg} at magnetic fields from 3 T to 9 T in step of 1 T. The linear relationship and negligible intercept clearly establishes $V_{sd}^* = \alpha \Delta V_{sg}$ with $\alpha = 4.5$ μ eV/mV. **e**, Zeeman splitting between subbands $|0,0,\downarrow\rangle$ and $|0,0,\uparrow\rangle$ with the same field variation in **d**. The g factor can be extracted to be $g = 0.6$. Remarkably, subbands $|0,0,\downarrow\rangle$ and $|0,0,\uparrow\rangle$ only split above a critical magnetic field $B_p = 1.1$ T, which is marked by the intercept in the B axis.

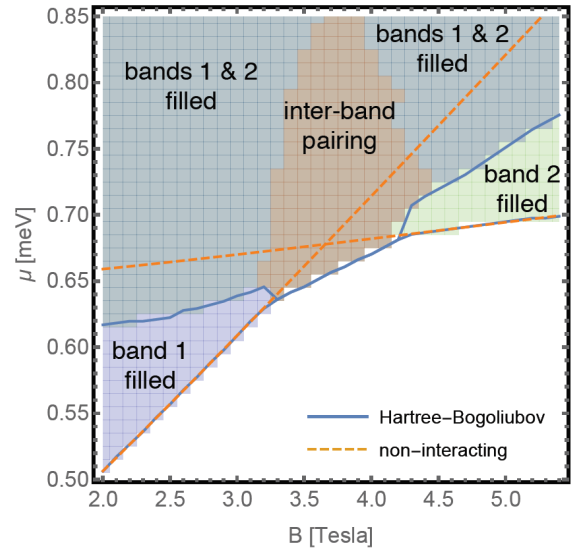


Figure 7 | Phase diagram of the Hartree-Bogoliubov model in the $\mu - B$ plane and near the crossing point of $|0, 1, \downarrow\rangle$ and $|1, 0, \uparrow\rangle$. In producing this diagram we used the band parameters for device A and set the attractive interaction constants to be $U_H = U_B = 100 \mu\text{eV}$.

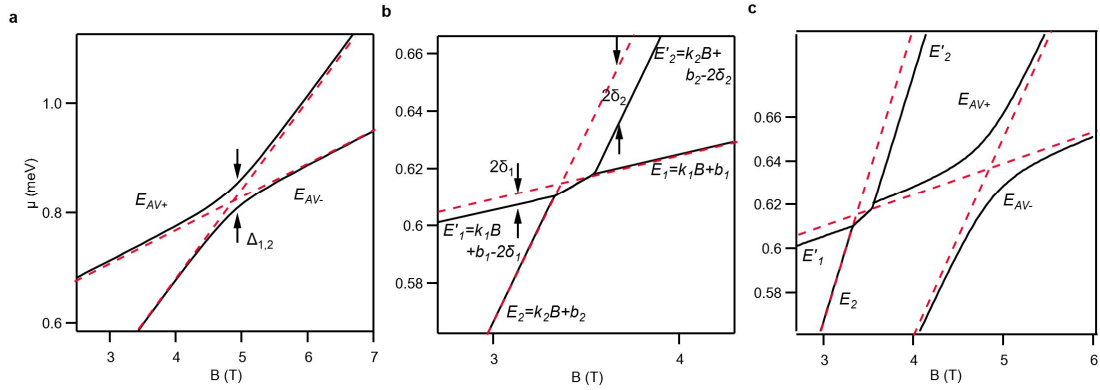


Figure 8 | Avoided crossing and re-entrant pairing model. **a**, Avoided crossing model. Two subbands of the same spin anti-cross when tuned to the same energy level. **b**, Re-entrant pairing model. Electrons in two subbands of opposite spins form a re-entrant pair when tuned to the same energy level at finite magnetic field. **c**, Combined model. The actual energy of subbands can be affected by both re-entrant pairing and avoided crossing. All the plots are based on device A.

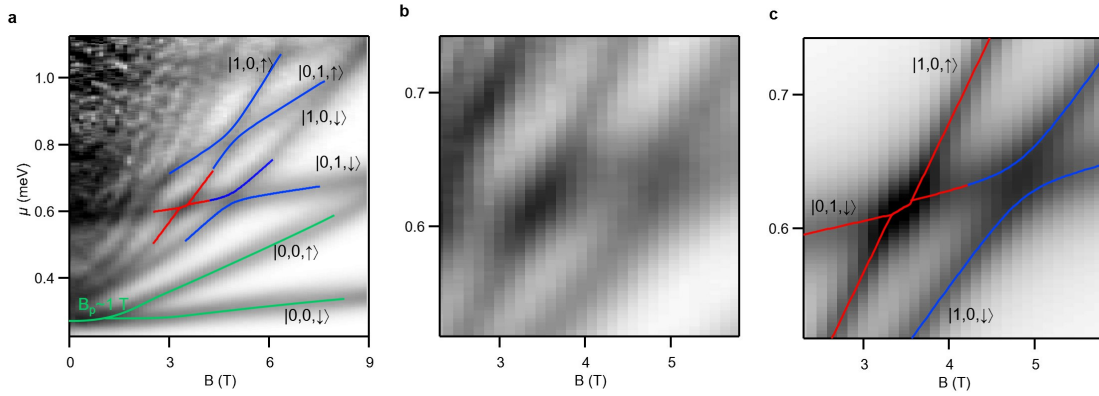


Figure 9 | Electron-electron interaction in device A. **a**, Electron pairing (green lines), avoided crossing (blue lines) and re-entrant pairing (red lines) fittings of device A. **b**, Detailed view of re-entrant pairing and avoided crossing data in (A). **c**, Combined model fitting of data shown in **b**. Here the red lines shows the fitting of re-entrant pairing between subband $|0,1,\downarrow\rangle$ and $|1,0,\uparrow\rangle$, with $\Delta_{rp} = 13 \mu\text{eV}$. The blue lines are fitting to the avoided crossing between subband $|0,1,\downarrow\rangle$ and $|1,0,\downarrow\rangle$, with $\Delta_{1,2} = 16 \mu\text{eV}$.

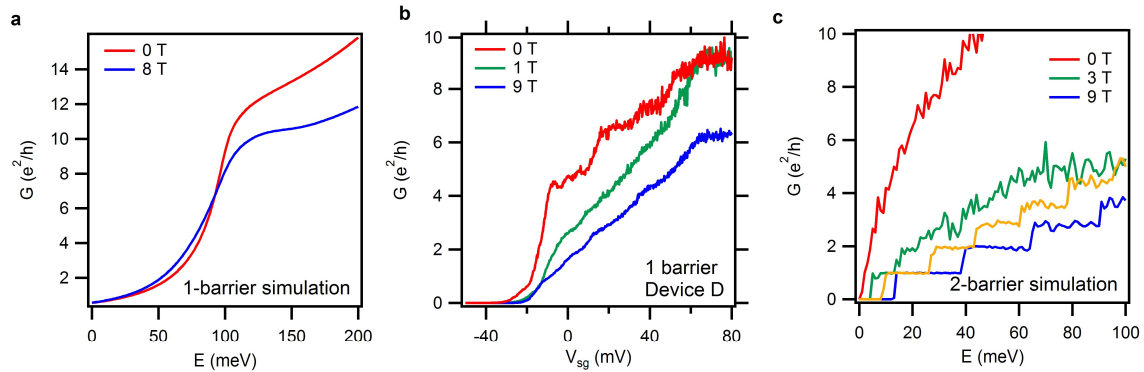


Figure 10 | Single barrier vs double barriers. **a**, Single barrier simulation. Conductance quantization is smeared by tunneling directly across the barrier (from source to drain). **b**, Transport data of device D with only one barrier. No precise conductance quantization is observed at all magnetic fields, qualitatively in agreement with **a**. The high conductance at zero field is likely due to superconductivity. **c**, Double barrier simulation. Two barriers isolate the electron waveguide from the leads and allow the side gate to tune the chemical potential. Direct tunneling from source to drain is also suppressed. Clear conductance quantization is observed at high magnetic fields.

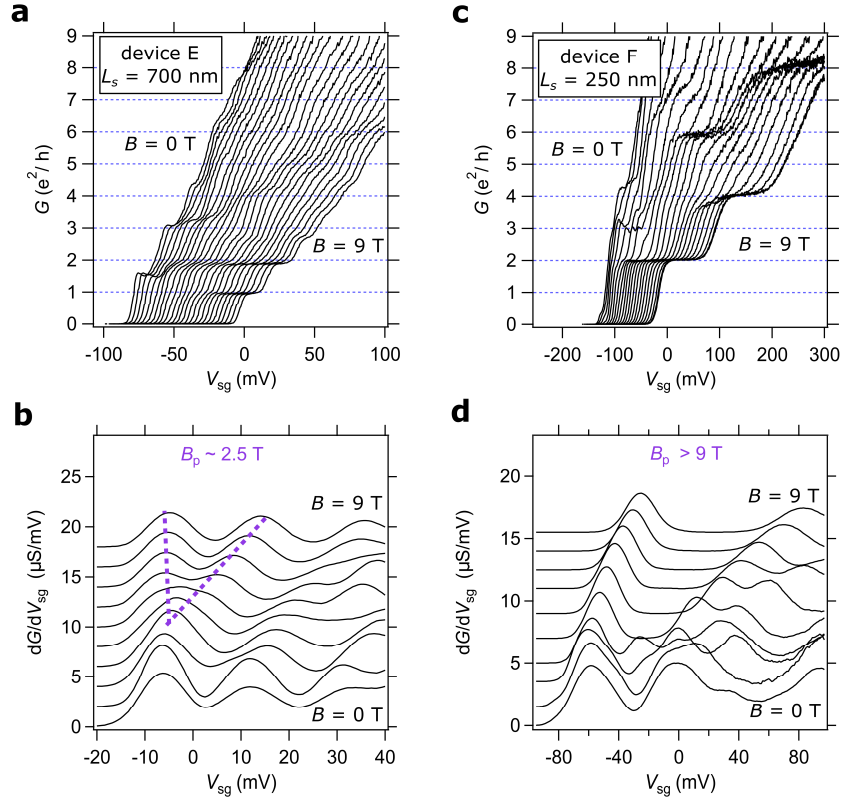


Figure 11 | Critical magnetic field for splitting the lowest two spin subbands for additional devices E and F. (a and c) Zero-bias conductance G as a function of V_{sg} and B for device D ($L_s = 700$ nm) and E ($L_s = 250$ nm) fabricated on different samples. Curves are offset for clarity. (b and d) Corresponding transconductance dG/dV_{sg} plots to reveal B_p at which subbands $|0,0, \downarrow\rangle$ and $|0,0, \uparrow\rangle$ start to split. B_p values are high for device E (~ 2.5 T) and F (> 9 T) compared to device A and B in the main text.

Table 1 | Avoided crossing fitting parameters for device A and B.

Device	Subbands	k ($\mu\text{eV}/\text{T}$)	b (μeV)	$\Delta_{1,2}$ (μeV)
Device A	$ 1,0,\uparrow\rangle$	167	8	20
	$ 0,1,\uparrow\rangle$	58	534	
	$ 1,0,\downarrow\rangle$	91	195	16
	$ 0,1,\downarrow\rangle$	15	566	
Device B	$ 1,0,\uparrow\rangle$	166	-58	34
	$ 0,1,\uparrow\rangle$	63	529	
	$ 1,0,\downarrow\rangle$	95	139	40
	$ 0,1,\downarrow\rangle$	14	585	

Table 2 | Re-entrant pairing fitting parameters for device A and B.

Device	Subbands	k ($\mu\text{eV}/\text{T}$)	b (μeV)	Δ_{rp} (μeV)
Device A	$ 1,0,\uparrow\rangle$	133	168	13
	$ 0,1,\downarrow\rangle$	15	566	
Device B	$ 1,0,\uparrow\rangle$	130	120	10
	$ 0,1,\downarrow\rangle$	14	585	

References

- [1] J. M. Luttinger, *Journal of Mathematical Physics* **4**, 1154 (1963).
- [2] T. Giamarchi, *Quantum Physics in One Dimension* (Oxford University Press, 2003).
- [3] O. M. Auslaender, H. Steinberg, A. Yacoby, Y. Tserkovnyak, B. I. Halperin, K. W. Baldwin, L. N. Pfeiffer, and K. W. West, *Science* **308**, 88 (2005).
- [4] H. Steinberg, G. Barak, A. Yacoby, L. N. Pfeiffer, K. W. West, B. I. Halperin, and K. Le Hur, *Nat Phys* **4**, 116 (2008).
- [5] R. Landauer, *IBM Journal of Research and Development* **1**, 223 (1957).
- [6] S. Frank, P. Poncharal, Z. L. Wang, and W. A. d. Heer, *Science* **280**, 1744 (1998).
- [7] Y.-M. Lin, V. Perebeinos, Z. Chen, and P. Avouris, *Physical Review B* **78**, 161409 (2008).
- [8] A. Yacoby, H. L. Stormer, N. S. Wingreen, L. N. Pfeiffer, K. W. Baldwin, and K. W. West, *Physical Review Letters* **77**, 4612 (1996).
- [9] I. van Weperen, S. R. Plissard, E. P. A. M. Bakkers, S. M. Frolov, and L. P. Kouwenhoven, *Nano Letters* **13**, 387 (2013).
- [10] G. Timp, A. M. Chang, P. Mankiewich, R. Behringer, J. E. Cunningham, T. Y. Chang, and R. E. Howard, *Physical Review Letters* **59**, 732 (1987).
- [11] F. D. M. Haldane, *Journal of Physics C: Solid State Physics* **14**, 2585 (1981).
- [12] C. L. Kane and M. P. A. Fisher, *Physical Review Letters* **68**, 1220 (1992).
- [13] T. Giamarchi and H. J. Schulz, *Physical Review B* **37**, 325 (1988).
- [14] A. Tsukazaki, S. Akasaka, K. Nakahara, Y. Ohno, H. Ohno, D. Maryenko, A. Ohtomo, and M. Kawasaki, *Nat Mater* **9**, 889 (2010).
- [15] A. Ohtomo and H. Y. Hwang, *Nature* **427**, 423 (2004).
- [16] S. Thiel, G. Hammerl, A. Schmehl, C. W. Schneider, and J. Mannhart, *Science* **313**, 1942 (2006).
- [17] N. Reyren *et al.*, *Science* **317**, 1196 (2007).
- [18] A. Brinkman *et al.*, *Nature Materials* **6**, 493 (2007).
- [19] M. Ben Shalom, M. Sachs, D. Rakhmilevitch, A. Palevski, and Y. Dagan, *Physical Review Letters* **104**, 126802 (2010).
- [20] A. D. Caviglia, M. Gabay, S. Gariglio, N. Reyren, C. Cancellieri, and J. M. Triscone, *Physical Review Letters* **104**, 126803 (2010).
- [21] P. Irvin, J. P. Veazey, G. Cheng, S. Lu, C.-W. Bark, S. Ryu, C.-B. Eom, and J. Levy, *Nano Letters* **13**, 364 (2013).
- [22] G. Cheng *et al.*, *Physical Review X* **3**, 011021, 011021 (2013).
- [23] A. Ron and Y. Dagan, *Physical Review Letters* **112**, 136801 (2014).
- [24] M. Tomczyk *et al.*, *Physical Review Letters* **117**, 096801 (2016).
- [25] C. Cen, S. Thiel, G. Hammerl, C. W. Schneider, K. E. Andersen, C. S. Hellberg, J. Mannhart, and J. Levy, *Nature Materials* **7**, 298, 10.1038/nmat2136 (2008).
- [26] A. Levy, F. Bi, M. Huang, S. Lu, M. Tomczyk, G. Cheng, P. Irvin, and J. Levy, *Journal of Visualized Experiments* **89**, e51886 (2014).
- [27] K. A. Brown *et al.*, *Nature Communications* **7**, 10681 (2016).

- [28] F. Bi, D. F. Bogorin, C. Cen, C. W. Bark, J. W. Park, C. B. Eom, and J. Levy, *Applied Physics Letters* **97**, 173110 (2010).
- [29] R. Dingle, H. L. Stormer, A. C. Gossard, and W. Wiegmann, *Applied Physics Letters* **33**, 665 (1978).
- [30] C. Rossler, S. Baer, E. de Wiljes, P. L. Ardel, T. Ihn, K. Ensslin, C. Reichl, and W. Wegscheider, *New Journal of Physics* **13**, 113006 (2011).
- [31] M. Salluzzo *et al.*, *Physical Review Letters* **102**, 166804, 166804 (2009).
- [32] M. A. Topinka, B. J. LeRoy, S. E. J. Shaw, E. J. Heller, R. M. Westervelt, K. D. Maranowski, and A. C. Gossard, *Science* **289**, 2323 (2000).
- [33] G. Cheng *et al.*, *Nature* **521**, 196 (2015).
- [34] G. Salis, T. Heinzel, K. Ensslin, O. J. Homan, W. Bachtold, K. Maranowski, and A. C. Gossard, *Physical Review B* **60**, 7756 (1999).
- [35] S. F. Fischer, G. Apetrii, U. Kunze, D. Schuh, and G. Abstreiter, *Physical Review B* **71**, 195330 (2005).
- [36] C. W. J. Beenakker and H. van Houten, *Physical Review Letters* **66**, 3056 (1991).
- [37] M. Kanasz-Nagy, L. Glazman, T. Esslinger, and E. A. Demler, (arXiv:1607.02509, 2016).
- [38] G. Cheng *et al.*, arXiv:1602.06029 (2016).
- [39] G. Cheng *et al.*, *Nat Nanotechnol* **6**, 343 (2011).
- [40] L. I. Glazman and A. V. Khaetskii, *Europhys Lett* **9**, 263 (1989).
- [41] Z. C. Zhong, A. Toth, and K. Held, *Physical Review B* **87**, 161102 (2013).
- [42] C. W. Groth, M. Wimmer, A. R. Akhmerov, and X. Waintal, *New Journal of Physics* **16**, 063065 (2014).
- [43] X.-W. Guan, M. T. Batchelor, and C. Lee, *Reviews of Modern Physics* **85**, 1633 (2013).
- [44] B. Wang, H.-D. Chen, and S. Das Sarma, *Phys Rev A* **79**, 051604 (2009).
- [45] G. Orso, E. Burovski, and T. Jolicoeur, *Physical Review Letters* **104**, 065301 (2010).